

Screening and further investigations on promising bi-functional catalysts for metal–air batteries with an aqueous alkaline electrolyte

Dennis Wittmaier · Timo Danner · Norbert Wagner ·
K. Andreas Friedrich

Received: 5 June 2013 / Accepted: 3 August 2013 / Published online: 25 August 2013
© Springer Science+Business Media Dordrecht 2013

Abstract A wide range catalyst screening with noble metal and oxide catalysts for a metal–air battery with an aqueous alkaline electrolyte was carried out. Suitable catalysts reduce overpotentials during the charge and discharge process, and therefore improve the round-trip efficiency of the battery. In this case, the electrodes will be used as optimized cathodes for a future lithium–air battery with an aqueous alkaline electrolyte. Oxide catalysts were synthesized via atmospheric plasma spraying. The screening showed that IrO_2 , RuO_2 , $\text{La}_{0.6}\text{Ca}_{0.4}\text{Co}_3$, Mn_3O_4 , and Co_3O_4 are promising bi-functional catalysts. Considering the high price for the noble metal catalysts further investigations of the oxide catalysts were carried out to analyze their electrochemical behavior at varied temperatures, molarities, and in case of $\text{La}_{1-x}\text{Ca}_x\text{CoO}_3$ a varying calcium content. Additionally all catalysts were tested in a longterm test to proof cyclability at varied molarities. Further investigations showed that Co_3O_4 seems to be the most promising bi-functional catalyst of the tested oxide

catalysts. Furthermore, it was shown that a calcium content of $x = 0.4$ in LCCO has the best performance.

Keywords Li–air battery · Oxygen reduction · Oxygen evolution · Bi-functional electrode · Alkaline electrolyte

1 Introduction

The worldwide increasing energy demand is predicted to double by 2030 (Fig. 1) and triple by 2050. In addition a fast growing number of combustion engine vehicles are putting pressure on prices, in particular on oil and ethanol.

The increasing emission of carbon dioxide is directly related to this growing demand of fossil fuel, and has reached almost 400 ppm in the atmosphere [2]. To decrease the emission of carbon dioxide, it is required to use more energy from renewable sources. Batteries are a high-efficient energy storage device for future energy systems based on renewable energy. Today's lithium-ion batteries (LIB) are limited in their capacity due to their active materials used on the anode and the cathode. The theoretical energy density of today's LIB's is only between 75 and 200 Wh kg⁻¹ [1, 3, 4]. Metal–air batteries and especially lithium–air batteries (LAB) have a far higher theoretical energy density compared to today's LIB's. Most researchers predict a five- to tenfold increase in energy density. The theoretical energy density of an aqueous LAB with metallic lithium used as an anode is 12,931 Wh kg⁻¹ [5], which is almost as high as the theoretical energy density of gasoline with approximately 13,200 Wh kg⁻¹. This high theoretical energy density cannot be achieved in practice due to limitations. Girishkumar et al. [3] estimate an energy density of 1,700 Wh kg⁻¹, which corresponds to

D. Wittmaier (✉) · T. Danner · N. Wagner · K. A. Friedrich
Institute of Technical Thermodynamics, German Aerospace
Center (DLR), Pfaffenwaldring 38-40, 70569 Stuttgart, Germany
e-mail: dennis.wittmaier@dlr.de

T. Danner
Helmholtz Institute Ulm for Electrochemical Energy Storage
(HIU), Ulm, Germany

T. Danner
Offenburg University of Applied Sciences, Offenburg, Germany

K. A. Friedrich
Institute for Thermodynamics and Thermal Engineering,
University of Stuttgart, Stuttgart, Germany

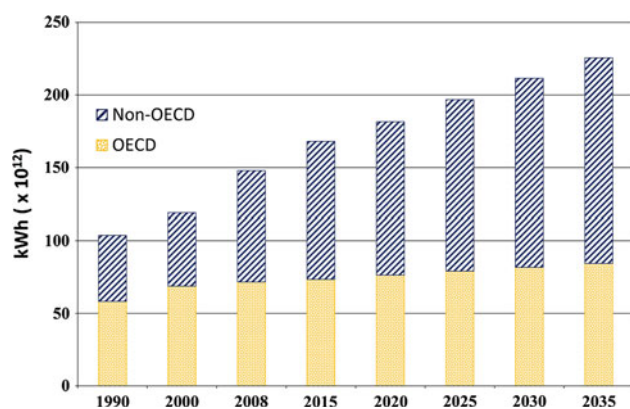
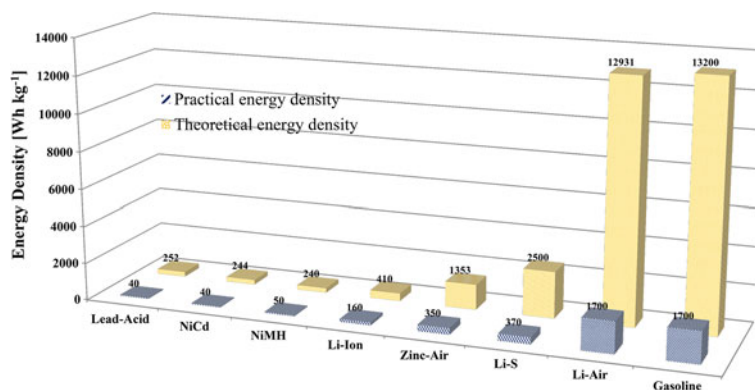


Fig. 1 World energy consumption [1]

13 % of the theoretical energy density of an aqueous LAB with a lithium-metal anode. This would be the same energy density that can be achieved with gasoline (Fig. 2).

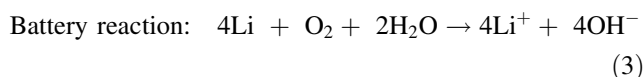
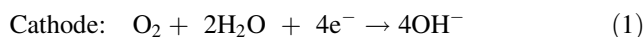
But there are still limiting factors that must be overcome before LAB can be used. Main limiting factors are the high overpotentials during charge and discharge. These are resulting mostly from insufficient bi-functional catalysts used on the cathode for the oxygen reduction reaction (ORR) while discharging, and the oxygen evolution reaction (OER) while charging. Furthermore, LAB's suffer from low cyclability and instable separators between the anode and cathode and the decomposition of used electrolytes. This paper deals with the synthesis and screening of suitable bi-functional catalysts for the use in cathodes of future LAB cells with aqueous alkaline electrolyte. In addition to established catalysts selected catalysts were taken from literature. Due to high costs of noble metal catalysts perovskite and spinel structure oxide catalysts have drawn attention recently [6–14]. After a screening test procedure the most promising perovskite and spinel catalysts namely $\text{La}_{0.6}\text{Ca}_{0.4}\text{CoO}_3$, Mn_3O_4 , and Co_3O_4 were further investigated. The focus was also on the electrochemical behavior of $\text{La}_{1-x}\text{Ca}_x\text{CoO}_3$ with a variable Ca content ($0.2 \leq x \leq 0.8$).

Fig. 2 Energy density of LAB compared to other batteries and gasoline [3]



2 Lithium–air batteries: architectures and electrochemical reactions

A lithium–air battery consists of a lithium-metal anode and a porous gas diffusion electrode on the cathode that contains at least one catalyst for the battery reaction. The two electrodes are separated by a lithium-ion conducting separator that protects the lithium-metal anode from oxygen and moisture. A protected lithium anode was recently proposed by Visco et al. [15], Zhang et al. [16], and Shimonishi et al. [17]. Worldwide research is focusing on four main cell architectures with different electrolytes. The all-solid-state, the aprotic, the aqueous, and mixed system with an aprotic electrolyte at the anode and an aqueous electrolyte at the cathode [3]. The electrochemistry depends on the electrolyte used at the cathode. In this paper cathodes for LAB's with an aqueous electrolyte, more specific with an alkaline electrolyte were investigated. The fundamental battery reactions are:

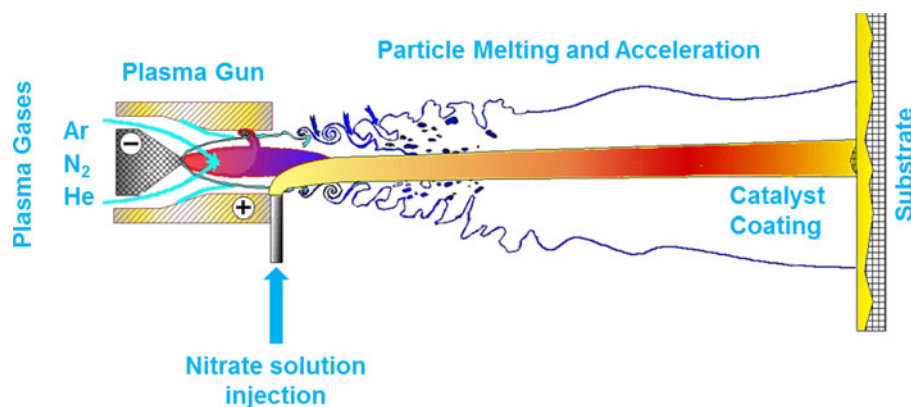


$$E_0 = 3.45 \text{ V}$$

While discharging O_2 is reduced at the cathode, according to Eq. 1. Simultaneously lithium is oxidized at the anode liberating lithium ions and electrons (Eq. 2). Equation 3 represents the overall battery reaction.

Selected catalysts were used to prepare electrodes and were tested in a half cell using cyclic voltammetry for analyzing the electrochemical performance of the catalysts. Longterm tests show the longterm stability of selected catalysts. XRD and SEM were used to investigate the morphology of the catalysts and the electrodes, respectively.

Fig. 3 Synthesis of catalysts via APS (modified from [18])



3 Experimental

Synthesis of catalysts, preparation of electrodes, experimental setup, and characterization methods will be described in this chapter.

3.1 Noble metal catalysts

The noble metal catalysts used were unsupported commercial noble metal nano-powders (>99 %; ChemPur, Sigma Aldrich, Umicore).

3.2 Synthesis of perovskite and spinel catalysts

Beside noble metal catalysts perovskite structure catalysts with the general formula $A_{1-x}A'_xB_{1-y}B_yO_3$ and spinel structure catalysts were screened for their suitability as bi-functional catalysts in LAB's with an aqueous alkaline electrolyte. These catalysts were synthesized via atmospheric plasma spraying (APS). Therefore, nitrates (>99 %, Alfa Aesar) were solved in demineralized water (0.3 M ratio) as a precursor. The nitrate solution was injected in the plasma jet of the DLR Triplex (SulzerMetco), where the nitrate solution was transformed into molten oxide catalyst splats. These splats were deposited on a pre-heated electrode substrate (Fig. 3).

The gas mixture for the plasma was argon (70 slm) and helium (35 slm). For the further examination of the oxide catalysts Mn_3O_4 , Co_3O_4 , and $La_{1-x}Ca_xCoO_3$ ($0 \leq x \leq 0.8$) were synthesized in the same way.

3.3 Preparation of electrodes

The noble metal electrodes were made by mixing Timrex T150 Graphite (Timcal) with Hostaflon TF2053 PTFE (3 M) as a binder in a ratio of 80:20 wt% and adding 1 mg catalyst per cm² electrode area. The powder mixture of graphite/binder/catalyst was pressed on a Sigracet[®] GDL 35DC (SGL Carbon) gas diffusion layer with a hydraulic press (Fig. 4a). The overall loading of all electrodes was 0.7 g to realize thin catalyst layer that reduces the influence

of the catalyst layer structure on the performance of the electrodes. Oxide catalyst layers were plasma sprayed on a stainless steel meshwork (Rhodius) (Fig. 4b).

3.4 Electrochemical characterizations

The electrochemical tests were carried out in a half-cell with a three electrode setup (Fig. 5).

In this setup, the noble metal catalyst or oxide catalyst electrode is the working electrode. A platinum electrode is used as counter electrode. The electrochemical potential was measured between the working electrode and a HydroFlex reversible hydrogen electrode (RHE, Gaskatel) as

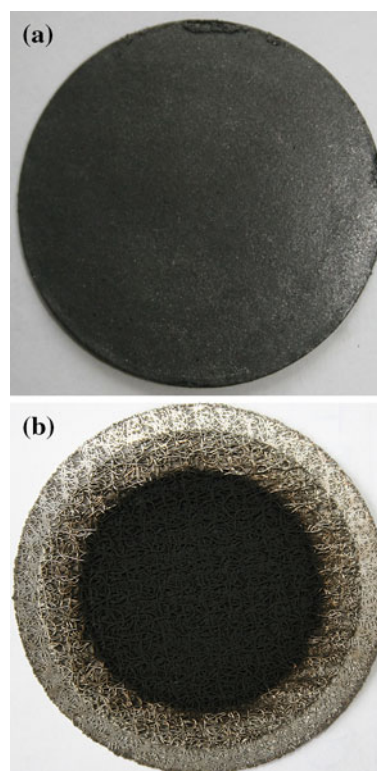


Fig. 4 **a** Gas diffusion electrode with noble metal catalyst on a Sigracet[®] GDL 35DC. **b** Oxide catalyst electrode on a stainless-steel meshwork

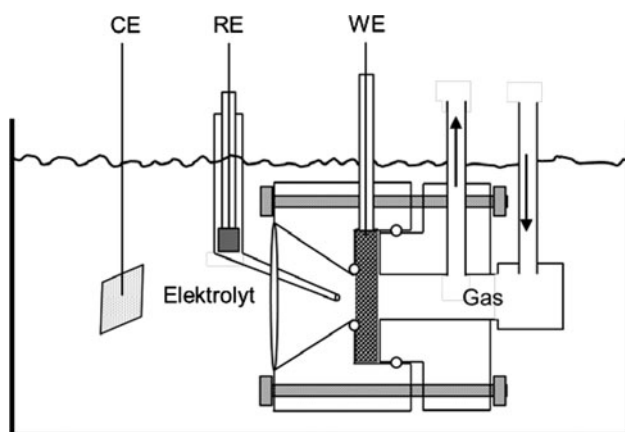


Fig. 5 Half-cell with a three electrode setup in electrolyte tank

reference electrode. The half-cell reduces the active area of the test electrode to 1 cm^2 . To reduce contact resistance between the Rhodium substrate used for the oxide catalyst electrodes and the current collector of the half-cell these electrodes were additionally stacked with a Sigracet® GDL 35DC on the gas side (Fig. 6).

In addition, this GDL is a hydrophobic layer which prevents the gas inlet from flooding with aqueous electrolyte. For the screening the half-cell was put into a electrolyte tank filled with 1,000 ml 1 M LiOH (aq.) (Fig. 5). The testing gas was purified oxygen (O_2). Cyclic voltammograms (CV) were carried out with a Zahner IM6 Electrochemical Workstation. The potential range for the screening was 0.1–1.8 V versus RHE and temperatures were varied in two steps 25 and 50 °C, respectively. The slow rate for all CVs was 1 mV s^{-1} . For the further investigations of the promising oxide catalysts the potential range was adapted to 0.5–1.8 V, to have an almost symmetric potential range coming from theoretical OCV. Furthermore the same temperature steps were used and the electrolyte was varied in the steps 0.1 and 1 M LiOH (aq.)

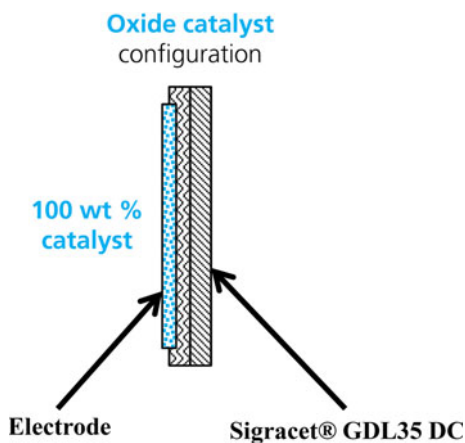


Fig. 6 Electrode configuration of a tested oxide catalyst electrode

to obtain the dependency of molarity on the performance of the catalysts. A longterm test with 75 cycles and ICP analysis of the electrolyte used to proof the stability of the electrodes and catalysts, respectively.

3.5 Electrolyte

The electrolytes used [0.1 M and 1 M LiOH (aq.)] were prepared by solving LiOH powder (98 %, Alfa Aesar) in demineralized water at room temperature.

3.6 X-ray diffraction and scanning electron microscopy

The synthesized oxide catalysts were characterized by X-ray diffraction (XRD). Therefore, a Bruker D8 Discover GADDS with monochromatized Cu K_α radiation was used. Each diffraction pattern was measured in four frames with a step size of 23° , starting with $\theta_1 = \theta_2 = 12^\circ$ (Bragg–Brentano condition). The exposure time for each frame was 180 s. The morphology of the catalysts was examined using a Zeiss ULTRA plus SEM with Charge Compensation.

4 Results

4.1 Screening of catalysts

Table 1 shows a list of all screened catalysts. All oxide catalysts were synthesized with APS, while for the noble metal catalyst and their mixtures commercially available catalyst powders were used.

Figures 7 and 8 show polarization curves of the tested electrodes during initial screening. Noble metal catalysts exhibit good performance in ORR and a comparatively poor performance in OER except for IrO_2 and RuO_2 , respectively (Fig. 7). Both seem to be the best balanced noble metal catalysts for bi-functional use. Increasing the temperature from 25 to 50 °C shows a significant improvement in performance. Doubling the temperature to 50 °C almost doubles the current densities. The anodic polarization curves of IrO_2 as well as of $\text{IrO}_2/\text{TiO}_2$ have a fluctuating characteristic when it comes to higher current

Table 1 Catalysts of the screening

Catalysts screening		
$\text{La}_{0.6}\text{Ca}_{0.4}\text{CoO}_3$	$\text{La}_{0.6}\text{Ca}_{0.4}\text{Co}_{0.8}\text{Fe}_{0.2}\text{O}_3$	$\text{La}_{0.6}\text{Sr}_{0.4}\text{Fe}_{0.8}\text{Mn}_{0.2}\text{O}_3$
$\text{La}_{0.6}\text{Ca}_{0.4}\text{Fe}_{0.8}\text{Mn}_{0.2}\text{O}_3$	$\text{Cu}_{1.5}\text{Mn}_{1.5}\text{O}_4$	$\text{Cu}_{0.3}\text{Co}_{2.7}\text{O}_4$
Co_3O_4	Mn_3O_4	NiO
AgCo	Pt	Au
Ag	IrO_2	RuO_2
PtAg	PtAu	$\text{IrO}_2/\text{TiO}_2$
AuAg		

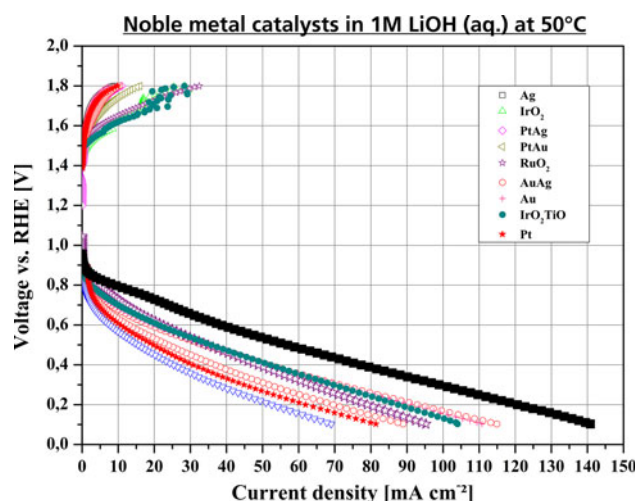


Fig. 7 Polarization curves of noble metal catalysts in 1 M LiOH (aq.) 50 °C

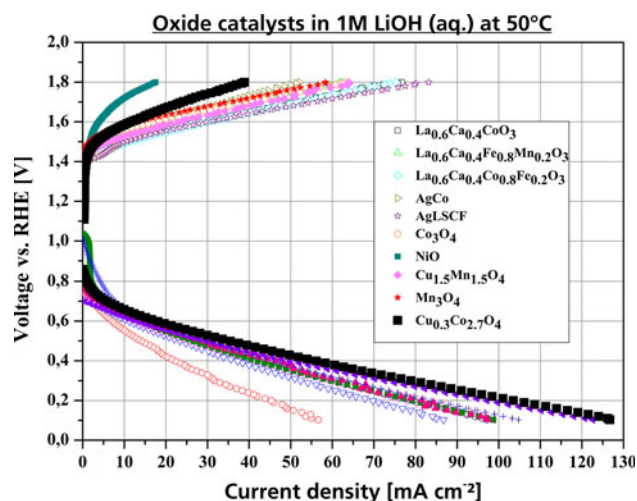
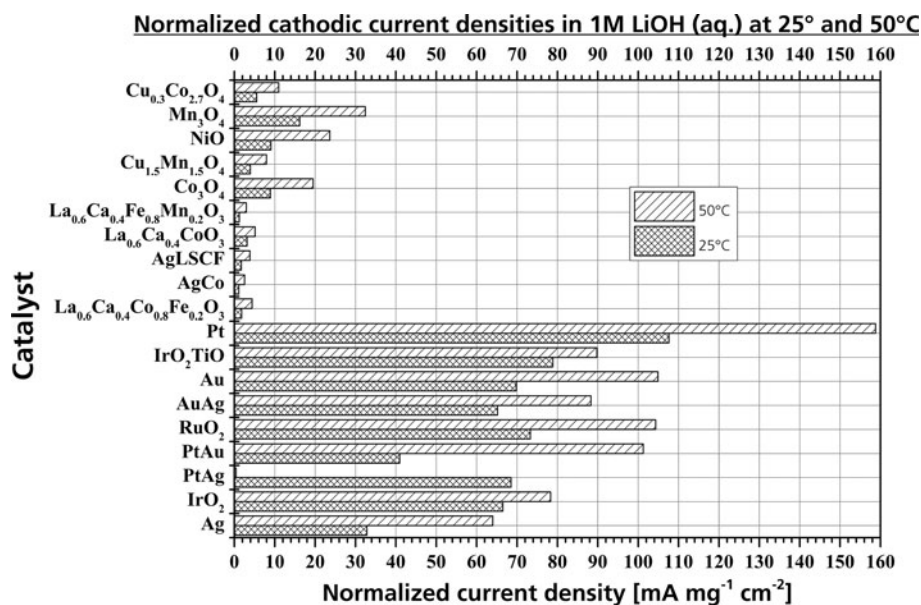


Fig. 8 Polarization curves of oxide catalysts in 1 M LiOH (aq.) 50 °C

Fig. 9 Normalized cathodic current densities at a potential of 0.3 V versus RHE [25 and 50 °C, 1 M LiOH (aq.)]



densities. This is due to the amount of evolved oxygen at the electrode. Growing oxygen bubbles adhere to the surface and block active sites on the surface and in the porous structure resulting in a decrease of the current density. Reaching a critical size, the oxygen bubbles come off the surface and the active site of the electrode is increased so is the current density. This is a repeating step during operation under oxygen evolution conditions [19]. Oxide catalyst exhibit more balanced characteristics toward ORR and OER than noble metal catalyst, but not exceeding current densities of noble metal catalyst electrodes (Fig. 8). Compared to their performances in ORR oxide catalysts show high performances in OER. Increasing the temperature from 25 to 50 °C shows also an improvement in current densities by factor two almost. Due to the fact that the catalyst loading is varying and the electrodes were made with two different manufacturing processes the current densities were normalized to mA cm^{-2} and mg catalyst loading to get comparable results (Figs. 9, 10). For comparison the current densities at 0.1 and 1.8 V versus RHE were taken as benchmark. Normalizing shows that RuO_2 , IrO_2 , Co_3O_4 , Mn_3O_4 , and $\text{La}_{0.6}\text{Ca}_{0.4}\text{CoO}_3$ seem to be the best catalysts for the use in LAB. They all show good performance in ORR as well as in OER.

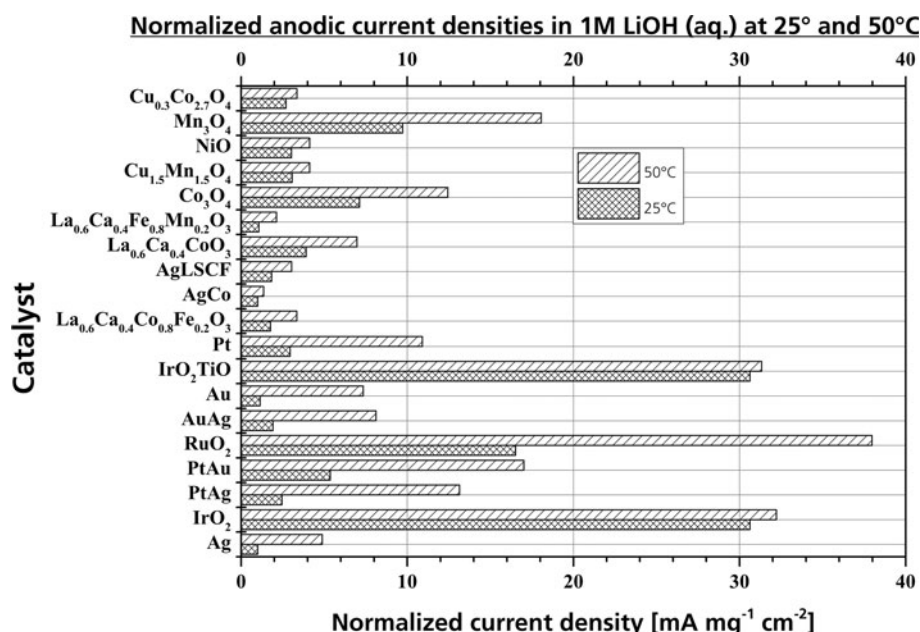
Considering the high price for RuO_2 and IrO_2 further investigations of the more inexpensive perovskite and spinel catalysts as an alternative to noble metals were carried out.

4.2 Further investigations of promising catalysts:

Co_3O_4 , Mn_3O_4 , $\text{La}_{1-x}\text{Ca}_x\text{CoO}_3$

The results of the further investigations are shown below.

Fig. 10 Normalized anodic current densities at a potential of 1.8 V versus RHE [25 and 50 °C, 1 M LiOH (aq.)]



4.2.1 XRD

Beside Co_3O_4 and Mn_3O_4 , the perovskite-type catalysts $\text{La}_{1-x}\text{Ca}_x\text{CoO}_3$ ($0 \leq x \leq 0.8$) were investigated. As for the screening, all catalysts were synthesized via APS. The XRD patterns of the perovskite type $\text{La}_{1-x}\text{Ca}_x\text{CoO}_3$ ($0 \leq x \leq 0.8$) do not change their general aspect of the pattern due to the changing calcium-content. They all show the LaCoO_3 structure. This was also seen by Kahoul et al. [20]. However, EDX proved the calcium-content in plasma sprayed electrodes, as can be seen in Figs. 11 and 12 for $\text{La}_{0.6}\text{Ca}_{0.4}\text{CoO}_3$.

With $x > 0.4$, the XRD patterns show an increasing content of parasitic phases. The amount of material with calcium lanthanum cobaltate structure is decreasing, while calcium cobaltate (Ca_3CoO_6) and La_2O_3 contents are increasing which have no perovskite structure [20]. Especially, La_2O_3 has a negative impact on the electrode performance. It is hygroscopic and it is dilating while absorbing water [21]. This leads to tensions in the catalyst layer and will end in peeling of the catalyst layer from the substrate used. Taking into account that the used electrolyte is an aqueous electrolyte catalysts containing a parasitic La_2O_3 phase cannot be used at any-time. Catalyst used must have a Ca-content $x \geq 0.4$. The spinel structures Co_3O_4 and Mn_3O_4 were also verified by XRD. Mn_3O_4 electrodes also showed a more inactive Mn_2O_3 phase.

4.2.2 Electrochemical tests

For the proof of the ability of the catalysts CVs were carried out resulting in polarization curves for the different

catalysts. Mn_3O_4 was found to be instable under testing conditions. The electrolyte used for Mn_3O_4 electrodes showed a change in color from without color to a yellow-colored electrolyte, which indicates a dissolution of manganese oxide in the electrolyte. Unfortunately longterm tests showed a significant loss of performance between cycles 1 and 25 which corresponds to the dissolution on catalyst material in the electrolyte (Fig. 13). Furthermore, the platinum electrode was coated with deposited manganese out of the electrolyte after cycling. This poor longterm stability because of dissolution in the electrolyte used makes Mn_3O_4 a unsuitable catalyst for future use in LAB with aqueous alkaline electrolyte.

More crystalline $\text{La}_{1-x}\text{Ca}_x\text{CoO}_3$ perovskites were found to favor the ORR, whereas more amorphous favor

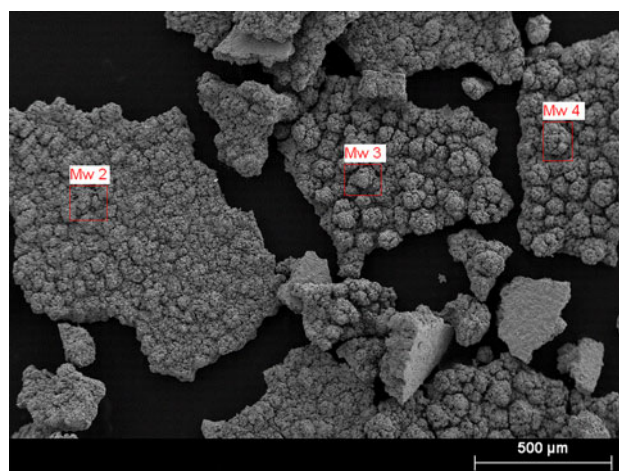


Fig. 11 SEM of EDX analyzed spots of $\text{La}_{0.6}\text{Ca}_{0.4}\text{CoO}_3$ electrodes

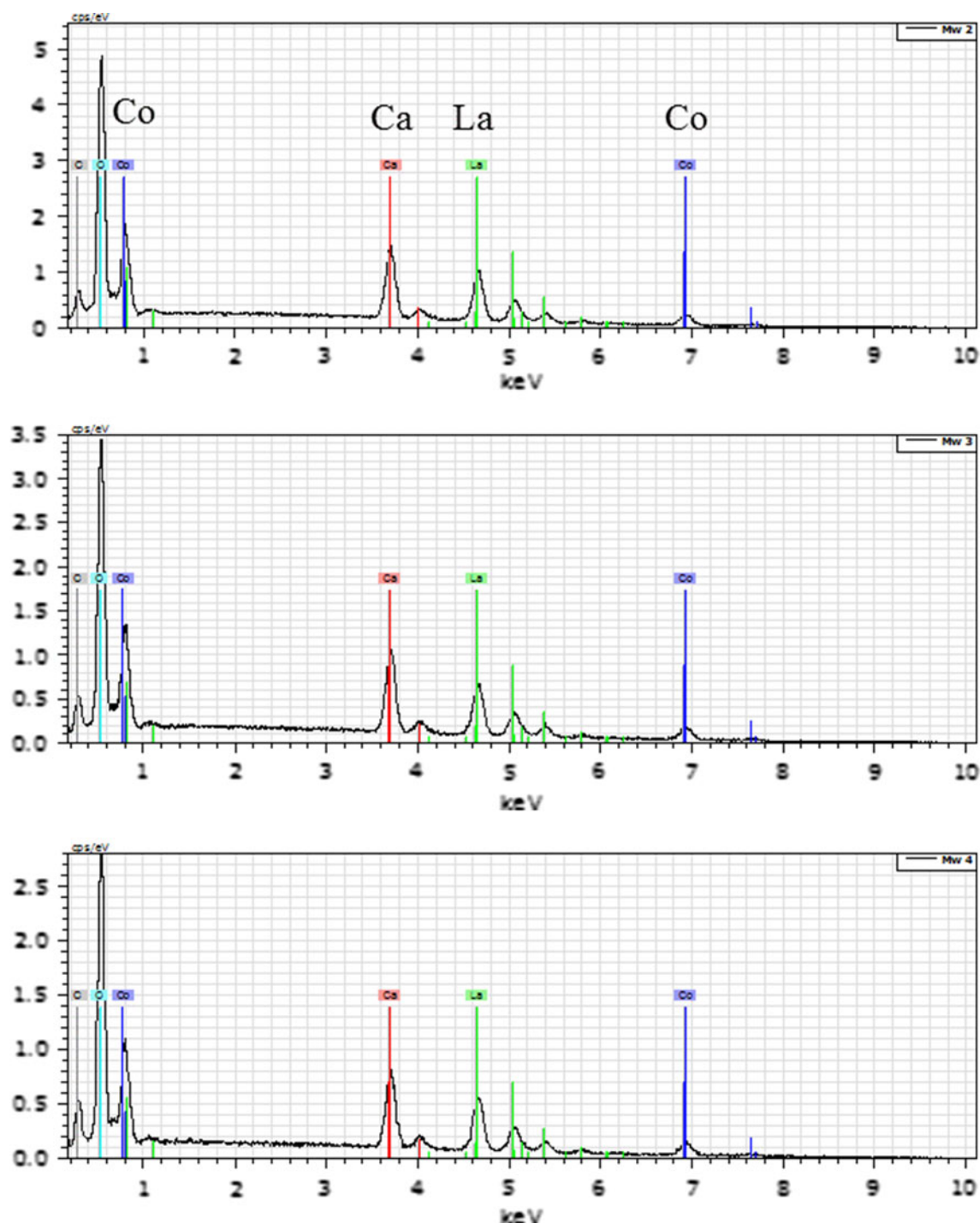


Fig. 12 EDX patterns of $\text{La}_{0.6}\text{Ca}_{0.4}\text{CoO}_3$ electrodes

OER [6, 22]. Also $\text{La}_{1-x}\text{Ca}_x\text{CoO}_3$ with $x = 0.2$ showed almost no improvement compared to $\text{La}_{1-x}\text{Ca}_x\text{CoO}_3$ $x = 0.4$ [6, 22]. The plasma sprayed $\text{La}_{1-x}\text{Ca}_x\text{CoO}_3$ perovskites showed a rather amorphous structure, while afterward when heat-treated it exhibits crystalline structure (800 °C, 40 h, ambient air). For $x = 0.4$ CVs were carried out with electrodes coated with the crystalline and the amorphous structure. Crystalline structure

electrodes exhibited a lower cycling performance than rather amorphous electrodes, but show a slightly higher ORR performance compared to OER performance at 25 °C (Fig. 14). Rather amorphous electrodes showed a better cycling performance and favor OER over ORR what corresponds to literature [6, 22]. For further investigations the electrodes with the rather amorphous structure were used.

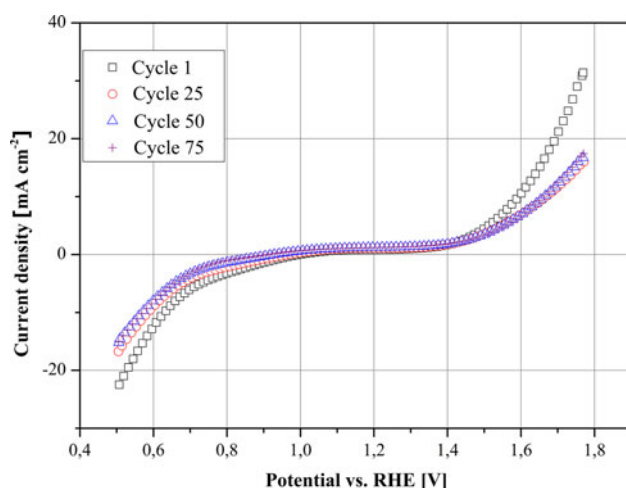


Fig. 13 Polarization curves of Mn_3O_4 electrodes over 75 cycles

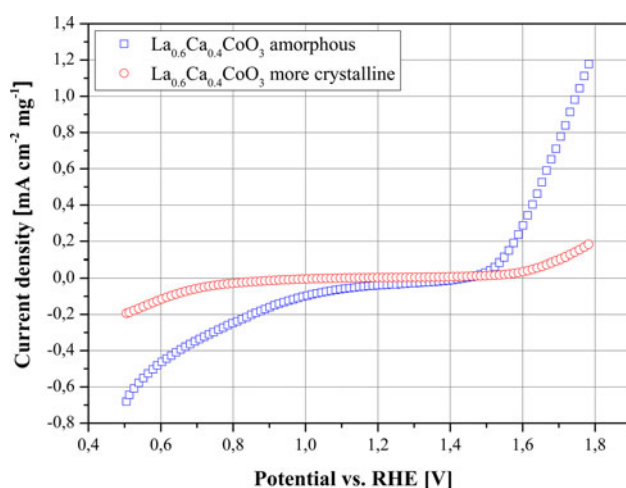


Fig. 14 Polarization curves of crystalline and amorphous electrodes in 1 M LiOH (aq.) at 25 °C

4.2.3 Polarization tests performed in 1 M LiOH (aq.)

$\text{La}_{0.6}\text{Ca}_{0.4}\text{CoO}_3$ shows best performance in ORR and OER at 25 and 50 °C. $\text{La}_{0.8}\text{Ca}_{0.2}\text{CoO}_3$ and LaCoO_3 show almost equal activities, but not exceed the performance of $\text{La}_{0.6}\text{Ca}_{0.4}\text{CoO}_3$. Ca-doping seems to favor ORR as well as OER with an optimum at $x = 0.4$. This is due to the decreasing resistivity through Ca-doping with a transformation from a semi-conductive to metallic conductivity [23]. But even $\text{La}_{0.6}\text{Ca}_{0.4}\text{CoO}_3$ has a low overall performance compared to the spinels Mn_3O_4 and Co_3O_4 . In fact, Co_3O_4 shows the best overall performance even though Mn_3O_4 shows a slightly higher performance in ORR (Fig. 15). But, as already mentioned, the degradation seen in the longterm tests have a great impact on performance.

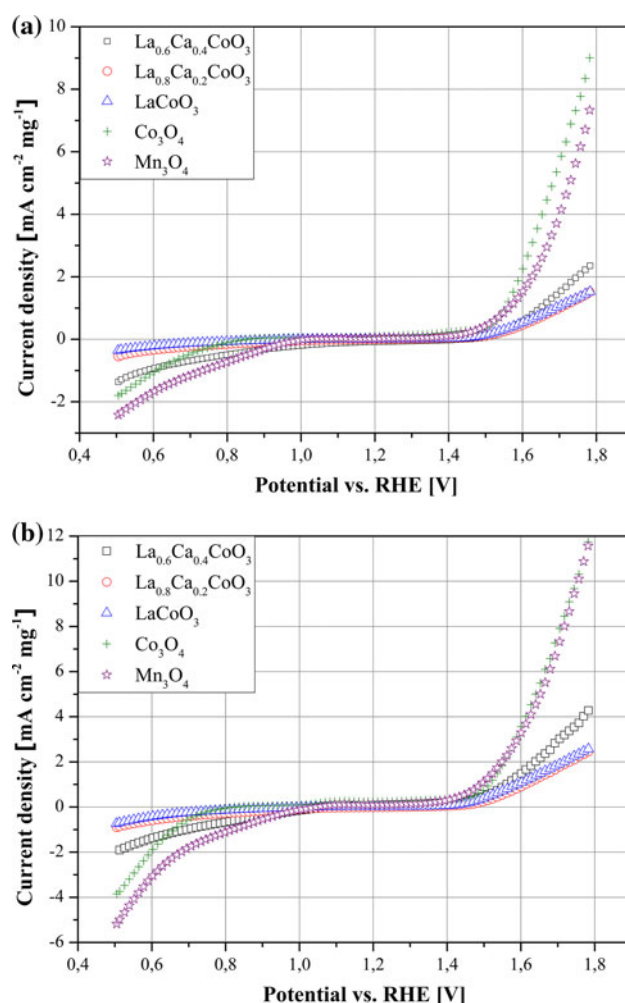


Fig. 15 Polarization curves of electrodes at **a** 25 °C and **b** 50 °C in 1 M LiOH (aq.)

Longterm tests show the cyclability of the perovskites and the spinels Co_3O_4 and Mn_3O_4 . Since, $\text{La}_{0.6}\text{Ca}_{0.4}\text{CoO}_3$ and Co_3O_4 are stable and show the best performance there is a special focus on these longterm tests.

$\text{La}_{0.6}\text{Ca}_{0.4}\text{CoO}_3$ shows a decrease in OER performance between cycles 1 and 50 at 50 °C (25 % of initial performance), but almost no loss in performance after cycle 50. So $\text{La}_{0.6}\text{Ca}_{0.4}\text{CoO}_3$ seems to be stable after the initial loss. ORR performance looks different. In fact, the initial ORR performance is the lowest and performance improved throughout cycling by 27.3 %. The other compositions of the $\text{La}_{1-x}\text{Ca}_x\text{CoO}_3$ perovskites exhibit a higher decrease of performance compared to $\text{La}_{0.6}\text{Ca}_{0.4}\text{CoO}_3$ and for both reactions ORR as well as OER. Mn_3O_4 , on the other hand, loses 49 % of its initial performance within the first 25 cycles, but shows a constant activity afterward, as already shown in Fig. 13. In ORR there is a loss of about 30 % of the initial activity. The overall losses are due to the dissolution of Mn_3O_4 in the electrolyte. Co_3O_4 exhibits a very stable

behavior for OER. Cycles 1 and 75 show almost the same performance. Actually the performance at cycle 75 is 3.4 % higher than in the initial cycle. ORR performance shows a degradation over 75 cycles of 61 %, but

still shows the same performance as $\text{La}_{0.6}\text{Ca}_{0.4}\text{CoO}_3$. Considering that Co_3O_4 is stable under alkaline conditions the degradation in ORR might be due to the formation of oxidation products on the surface not

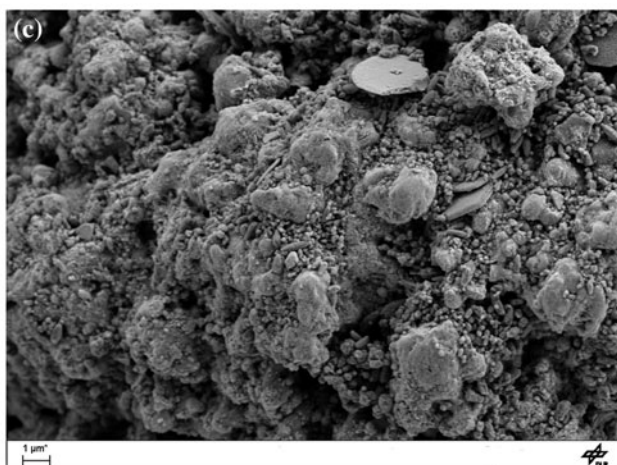
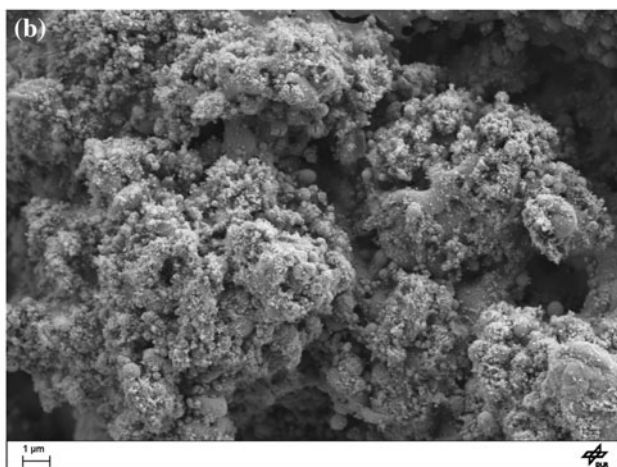
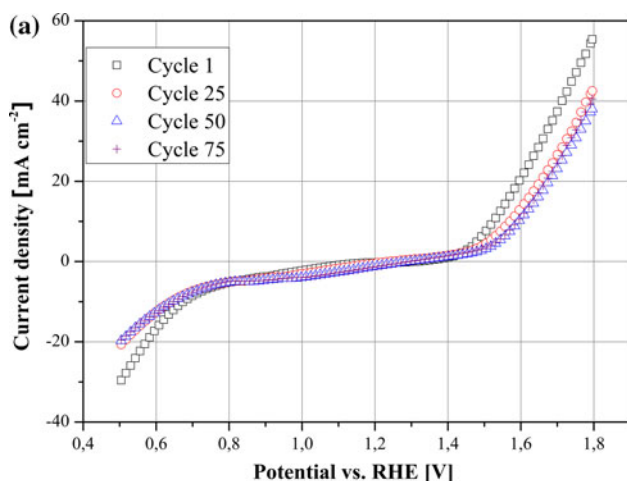


Fig. 16 LaCoO_3 electrode **a** polarization curves of cycle 1, 25, 50, and 75, **b** pristine electrode, and **c** after cycling

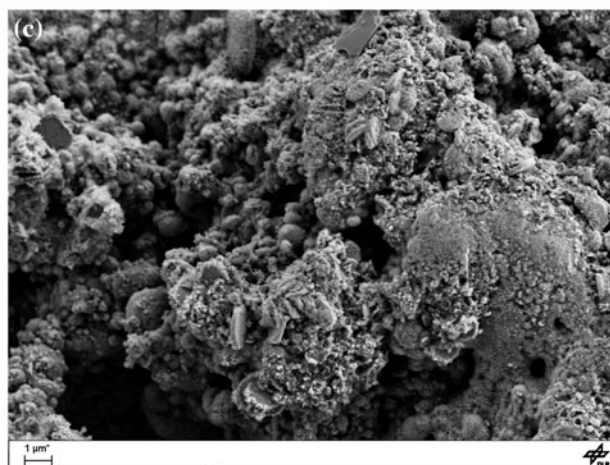
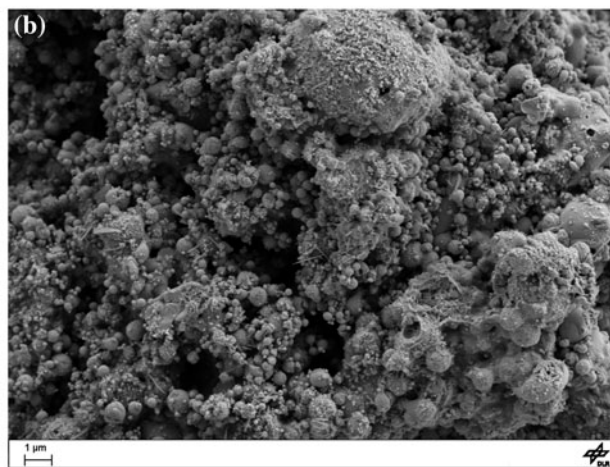
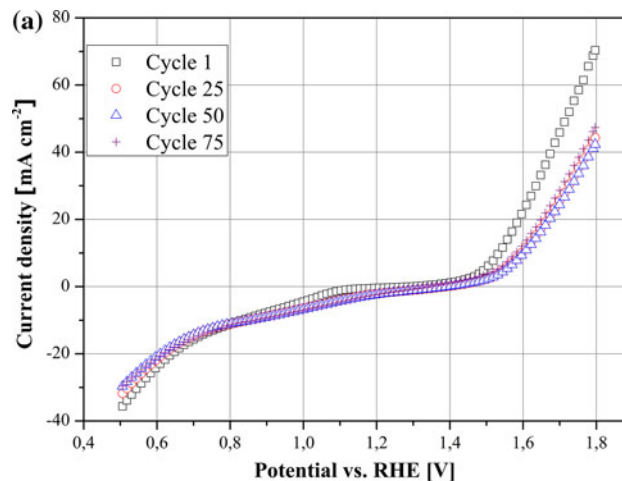


Fig. 17 $\text{La}_{0.8}\text{Ca}_{0.2}\text{CoO}_3$ electrode **a** polarization curves of cycle 1, 25, 50, and 75, **b** pristine electrode, and **c** after cycling

completely reduced in cathodic operation mode. The ORR as well as the OER at the perovskites starts with lower overpotentials coming from OCV than at Co_3O_4 . Co_3O_4 shows a distinctive potential plateau around OCV before it starts to catalyzing either oxygen reduction or

evolution. Figures 16, 17, 18, and 19 illustrate polarization curves of the longterm tests of each electrode as well as SEM images of the pristine and cycled electrode.

As one can see from the SEM images the decrease of the performances is due to morphologic changes of the

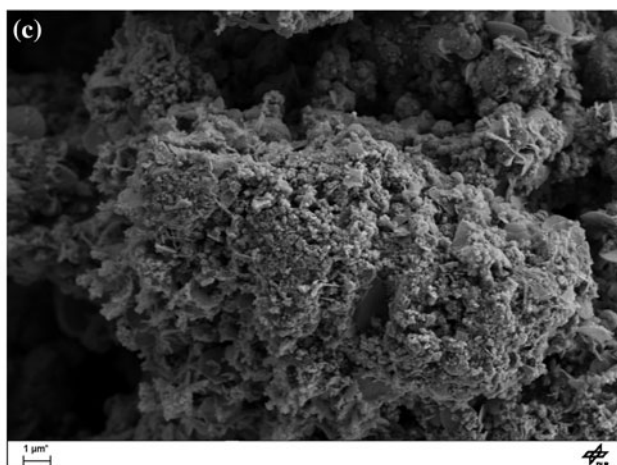
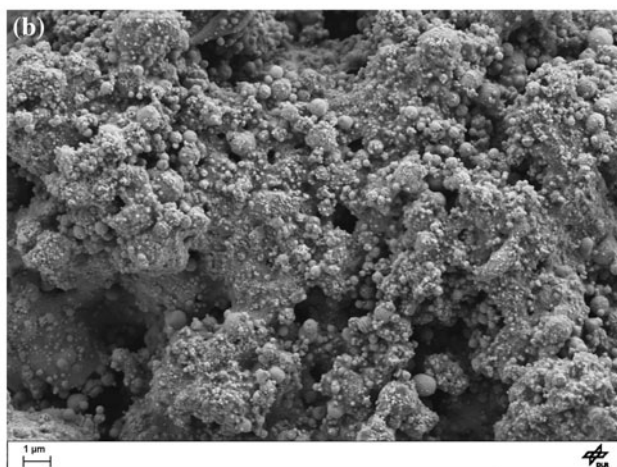
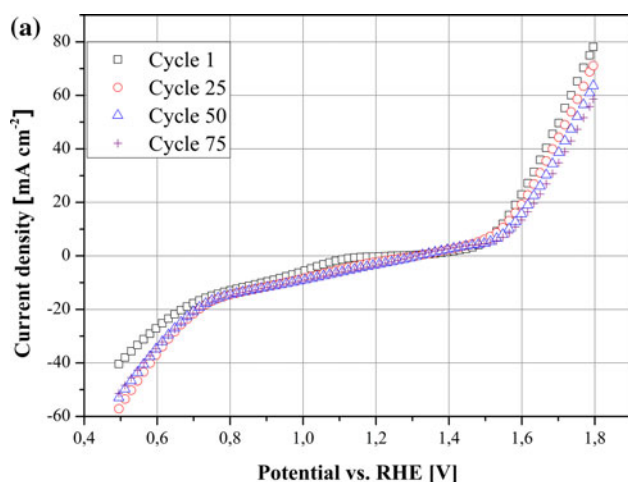


Fig. 18 $\text{La}_{0.6}\text{Ca}_{0.4}\text{CoO}_3$ electrode **a** polarization curves of cycle 1, 25, 50, and 75, **b** pristine electrode, and **c** after cycling

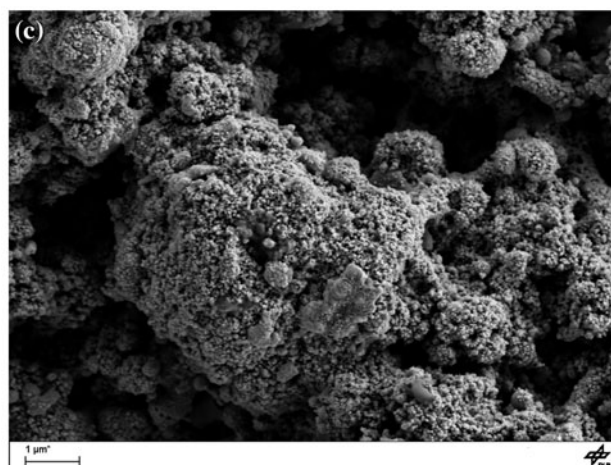
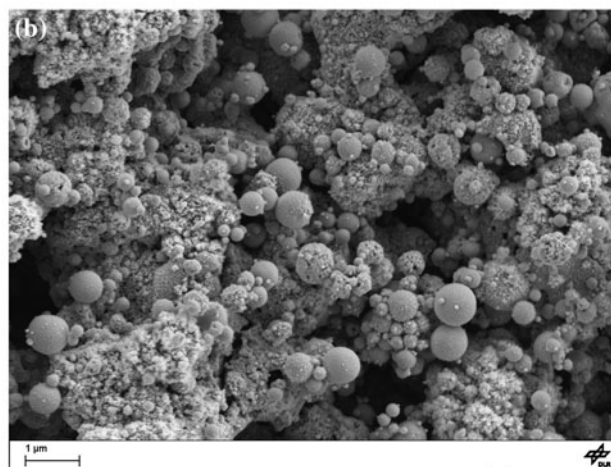
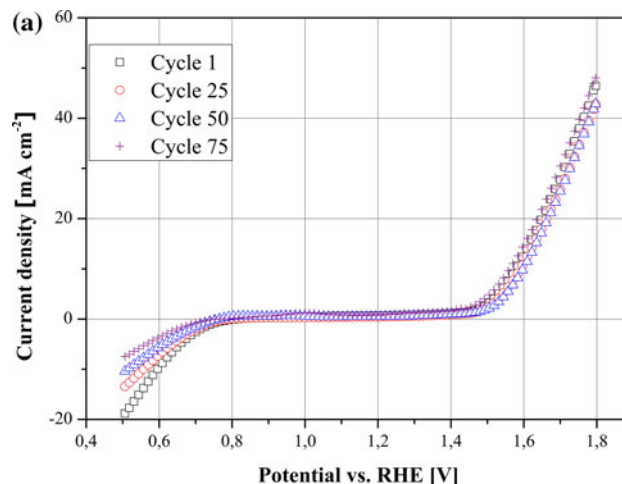
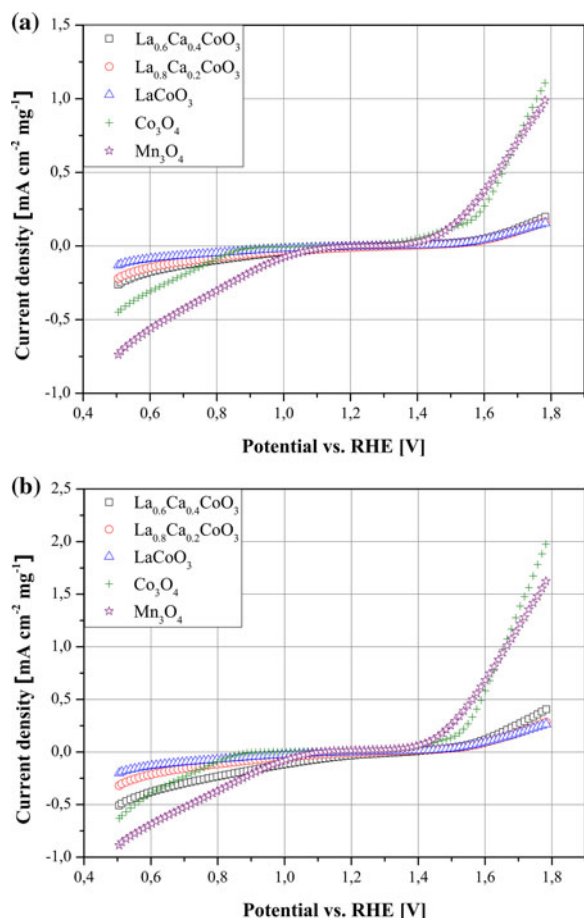


Fig. 19 Co_3O_4 electrode **a** polarization curves of cycle 1, 25, 50, and 75, **b** pristine electrode, and **c** after cycling

Table 2 Current densities normalized to $\text{mA cm}^{-2} \text{mg}^{-1}$ of longterm test electrodes

Molarity:	1 M							
Cycle:	1		25		50		75	
Mode:	Anodic	Cathodic	Anodic	Cathodic	Anodic	Cathodic	Anodic	Cathodic
Co_3O_4	11.50	4.73	10.80	3.38	10.80	2.61	11.80	1.88
Mn_3O_4	7.90	5.75	3.96	4.28	4.10	4.28	4.11	3.88
LaCoO_3	1.64	0.89	1.26	0.62	1.12	0.59	1.18	0.59
$\text{La}_{0.8}\text{Ca}_{0.2}\text{CoO}_3$	2.22	1.13	1.40	1.00	1.34	0.93	1.50	0.93
$\text{La}_{0.6}\text{Ca}_{0.4}\text{CoO}_3$	2.90	1.50	2.55	2.12	2.36	1.97	2.07	1.91

**Fig. 20** Polarization curves of electrodes at **a** 25 °C and **b** 50 °C in 0.1 M LiOH (aq.)

electrode surface. All electrodes show this change and there is a dependency on molarity of the LiOH (aq.) electrolyte, as can be seen in the next chapter.

Table 2 shows the maximum anodic and cathodic current densities of the longterm tests with 1 M LiOH (aq.).

4.2.4 0.1 M LiOH (aq.)

Decreasing the molarity from 1 to 0.1 M does not change the general aspect of the polarization curves, but has a great influence on the performance. $\text{La}_{0.6}\text{Ca}_{0.4}\text{CoO}_3$ still exhibits the best activity of the perovskites, while Co_3O_4 far exceeds the performances of the perovskites. The decrease of performances is mainly due to the increasing resistivity of the lower molar electrolyte [24]. Performances decrease by one order of magnitude which corresponds to the decrease in molarity (Fig. 20).

Table 3 shows the anodic and cathodic current densities of the electrodes tested in 0.1 M and 1 M LiOH (aq.).

4.2.5 Longterm tests in 0.1 M LiOH (aq.)

Longterm tests were also carried out with 0.1 M electrolyte. LaCoO_3 and $\text{La}_{0.8}\text{Ca}_{0.2}\text{CoO}_3$ show a slight degradation in OER over 75 cycles, while $\text{La}_{0.6}\text{Ca}_{0.4}\text{CoO}_3$ shows no noticeable degradation and seems to be the most stable perovskite tested. In contrast to the test in 1 M LiOH (aq.), Co_3O_4 remains stable for ORR and shows only a slight degradation for OER of 17.4 % over 75 cycles. Table 4 shows the maximum anodic and cathodic current densities,

Table 3 Current densities normalized to $\text{mA cm}^{-2} \text{mg}^{-1}$ of tested electrodes in 0.1 M and 1 M LiOH (aq.)

Molarity:	0.1 M				1 M			
Temperature (°C):	25		50		25		50	
Mode:	Anodic	Cathodic	Anodic	Cathodic	Anodic	Cathodic	Anodic	Cathodic
Co_3O_4	1.11	0.45	1.98	0.63	9.53	1.69	12.90	3.85
Mn_3O_4	0.99	0.74	1.62	0.88	7.33	2.42	11.60	5.18
LaCoO_3	0.15	0.13	0.26	0.20	1.53	0.36	2.57	0.73
$\text{La}_{0.8}\text{Ca}_{0.2}\text{CoO}_3$	0.17	0.22	0.27	0.32	1.42	0.55	2.45	0.90
$\text{La}_{0.6}\text{Ca}_{0.4}\text{CoO}_3$	0.20	0.26	0.41	0.50	2.22	1.36	4.28	1.90

Table 4 Current densities of longterm test electrodes normalized to $\text{mA cm}^{-2} \text{mg}^{-1}$

Molarity:	0.1 M							
Cycle:	1		25		50		75	
Mode:	Anodic	Cathodic	Anodic	Cathodic	Anodic	Cathodic	Anodic	Cathodic
Co_3O_4	2.00	0.71	1.78	0.73	1.68	0.75	1.65	0.75
Mn_3O_4	1.78	0.87	1.71	0.86	1.51	0.86	1.34	0.86
LaCoO_3	0.27	0.21	0.26	0.22	0.24	0.22	0.21	0.21
$\text{La}_{0.8}\text{Ca}_{0.2}\text{CoO}_3$	0.29	0.34	0.29	0.31	0.27	0.31	0.27	0.30
$\text{La}_{0.6}\text{Ca}_{0.4}\text{CoO}_3$	0.33	0.39	0.30	0.37	0.30	0.37	0.28	0.36

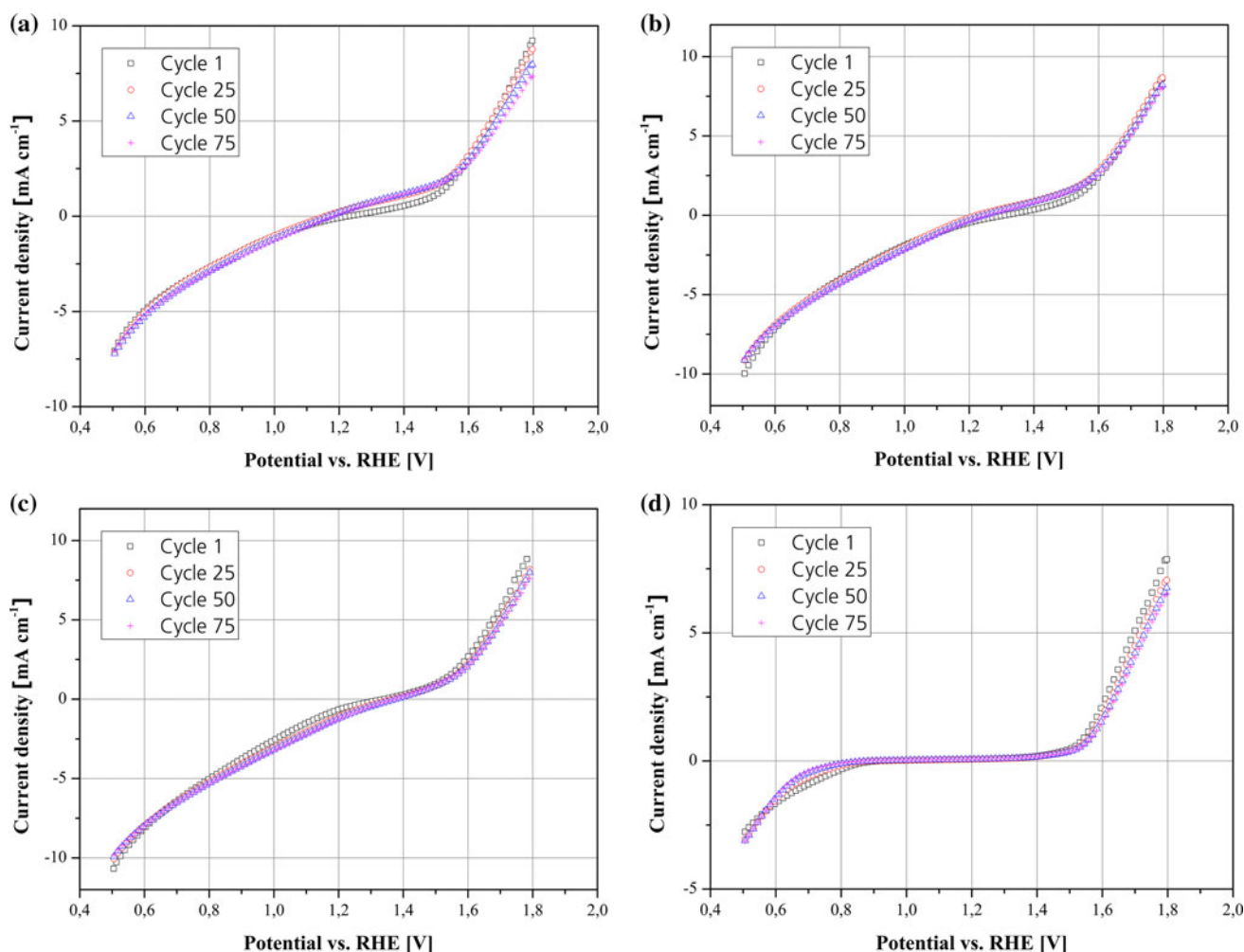


Fig. 21 **a** LaCoO_3 electrode polarization curves of cycle 1, 25, 50, and 75 in 0.1 M LiOH (aq.). **b** $\text{La}_{0.8}\text{Ca}_{0.2}\text{CoO}_3$ electrode polarization curves of cycle 1, 25, 50, and 75 in 0.1 M LiOH (aq.). **c** $\text{La}_{0.6}\text{Ca}_{0.4}\text{CoO}_3$ electrode polarization curves of cycle 1, 25, 50, and 75 in 0.1 M LiOH (aq.). **d** Co_3O_4 electrode polarization curves of cycle 1, 25, 50, and 75 in 0.1 M LiOH (aq.)

Fig. 21a–d shows the CVs of the longterm tests in 0.1 M LiOH (aq.).

Table 4 shows the maximum anodic and cathodic current densities of the longterm tests with 0.1 M LiOH (aq.).

5 Conclusions

A wide range screening yields to the catalysts $\text{La}_{0.6}\text{Ca}_{0.4}\text{CoO}_3$, Mn_3O_4 , and Co_3O_4 as possible catalysts for aqueous alkaline lithium–air batteries. The initial screening and

further investigations on the catalysts show a significant dependency of the performance on the temperature. Mn_3O_4 showed one of the best performances but is not stable in the alkaline electrolyte. A comparison of $\text{La}_{1-x}\text{Ca}_x\text{CoO}_3$ with ($0 \leq x \leq 0.8$) showed that Ca-doping enhances the performance of the electrodes with an optimum at $x = 0.4$. Molarity influences the performance because of the increasing resistivity in the cell with decreasing molarity. Molarity was also found to have an influence on the degradation of the electrodes. The decreasing performance seems to be due to the morphologic changes at the surface of the electrodes. Even though Co_3O_4 shows a comparable high degradation in ORR performance it seems to be the most promising catalyst.

Acknowledgments The authors would like to thank the Federal Ministry of Education and Research for funding this study. This study is part of the “LuftLi – Strom aus Luft und Lithium” project (FKZ:03X4624C).

References

1. International Energy Outlook (2011) U.S. Energy Information Administration (EIA)
2. Co_2Now . www.co2now.org. Accessed 21 May 2013
3. Girishkumar G, McCloskey B, Luntz AC, Swanson S, Wilcke W (2010) *J Phys Chem Lett* 1:2193
4. Padbury R, Zhang X (2011) *J Power Sources* 196:4436
5. Linden D, Reddy TB (2002) *Handbook of batteries*, 3rd edn. McGraw-Hill, New York, pp 38–46
6. Jörisen L (2006) *J Power Sources* 155:23
7. Song M, Park S, Alamgir FM, Cho J, Liu M (2011) *Mater Sci Eng* 72:203
8. Lu Y, Gasteiger HA, Parent MC, Chiloyan V, Shao-Horn Y (2010) *Electrochem Solid-State Lett* 13:A69
9. Lee CK, Striebel KA, McLarnon FR, Cairns EJ (1997) *J Electrochem Soc* 144:3801
10. Ohkuma H, Uechi I, Imanishi N, Hirano A, Takeda Y, Yamaoto O (2013) *J Power Sources* 223:319
11. Fukiwara N, Yao M, Siroma Z, Senoh H, Ioroi T, Yasada K (2011) *J Power Sources* 196:808
12. Chang Y, Wu P, Hsieh Y (2009) *J Power Sources* 189:1003
13. Neburchilov V, Wang H, Martin JJ, Qu W (2010) *J Power Sources* 195:1271
14. Nikolova V, Iliev P, Petrov K, Vitanov T, Zhecheva E, Stoyanova R, Valov I, Stoychev D (2008) *J Power Sources* 185:727
15. Visco S, Nimon E, Katz B, Chu M, Jonghe L (2012) Abstract #1156. Honolulu PRIME 2012, ECS
16. Zhang T, Nobuyuki A (2008) *J Electrochem Soc* 155:A965
17. Shimonishi Y, Zhang T, Imanishi N, Im D, Lee DJ, Hirano A, Takeda Y, Yamamoto O, Sammes N (2011) *J Power Sources* 196:5128
18. Fauchais P (2004) *J Phys D Appl Phys* 37:R86
19. Dinkelacker M (1989) PhD Thesis, University of Stuttgart
20. Kahoul A, Hammouche A, Naamoune F, Chartier P, Poillat G, Koenig JF (2000) *Mater Res Bull* 35(12):1955
21. Kwon J, Dai M, Halls MD, Langereis E, Chabal YJ, Gordon RG (2009) *J Phys Chem C* 113:654
22. Zhuang S, Liu S (2012) *Int J Electrochem Sci* 7:338
23. Kononyk IF, Tolochko SP, Lutsko VA, Anishchik VM (1983) *J Solid State Chem* 48:209
24. He P, Wang Y, Zhou H (2011) *J Power Sources* 196:5611